



Article

# Nanostructured Cu<sub>2</sub>O Synthesized via Bipolar Electrochemistry

Steven McWilliams<sup>1</sup>, Connor D. Flynn<sup>1</sup>, Jennifer McWilliams<sup>2</sup>, Donna C. Arnold<sup>3</sup> ,  
Ruri Agung Wahyuono<sup>4</sup>, Andreas Undisz<sup>5</sup>, Markus Rettenmayr<sup>5</sup> and Anna Ignaszak<sup>1,\*</sup> 

<sup>1</sup> Department of Chemistry, University of New Brunswick, Fredericton, NB E3B 5A3, Canada; Steven.McWilliams@unb.ca (S.M.); connor.flynn@unb.ca (C.D.F.)

<sup>2</sup> Department of Psychology, University of New Brunswick, Fredericton, NB E3B 5A3, Canada; Jennifer.Sanford@unb.ca

<sup>3</sup> School of Physical Sciences, University of Kent, Canterbury CT2 7NH, UK; d.c.arnold@kent.ac.uk

<sup>4</sup> Institute for Physical Chemistry and Abbe Center of Photonics, Friedrich-Schiller-Universität, 07743 Jena, Germany; ruri.wahyuono@uni-jena.de

<sup>5</sup> Otto Schott Institute of Materials Research, Chair of Metallic Materials, Friedrich-Schiller-Universität, 07743 Jena, Germany; Andreas.Undisz@uni-jena.de (A.U.); M.Rettenmayr@uni-jena.de (M.R.)

\* Correspondence: Anna.Ignaszak@unb.ca; Tel.: +1-506-261-9128

Received: 22 November 2019; Accepted: 12 December 2019; Published: 15 December 2019



**Abstract:** Cuprous oxide (Cu<sub>2</sub>O) was synthesized for the first time via an open bipolar electrochemistry (BPE) approach and characterized in parallel with the commercially available material. As compared to the reference, Cu<sub>2</sub>O formed through a BPE reaction demonstrated a decrease in particle size; an increase in photocurrent; more efficient light scavenging; and structure-correlated changes in the flat band potential and charge carrier concentration. More importantly, as-synthesized oxides were all phase-pure, defect-free, and had an average crystallite size of 20 nm. Ultimately, this study demonstrates the impact of reaction conditions (e.g., applied potential, reaction time) on structure, morphology, surface chemistry, and photo-electrochemical activity of semiconducting oxides, and at the same time, the ability to maintain a green synthetic protocol and potentially create a scalable product. In the proposed BPE synthesis, we introduced a common food supplement (potassium gluconate) as a reducing and complexing agent, and as an electrolyte, allowing us to replace the more harmful reactants that are conventionally used in Cu<sub>2</sub>O production. In addition, in the BPE process very corrosive reactants, such as hydroxides and metal precursors (required for synthesis of oxides), are generated in situ in stoichiometric quantity, providing an alternative methodology to generate various nanostructured materials in high yields under mild conditions.

**Keywords:** bipolar electrochemistry; green synthesis; substructure; photocurrent; semiconductors

## 1. Introduction

In recent years, cuprous oxide (Cu<sub>2</sub>O) has become increasingly popular as a semiconductor given its dual ability to convert solar energy and facilitate the photoelectrochemical splitting of water in photovoltaic devices [1,2]. While promising as a semiconductor, the major shortcoming that restricts the application of Cu<sub>2</sub>O in photovoltaics is its photochemical instability [3,4]. Numerous studies have been devoted to improving the stability of Cu<sub>2</sub>O electrodes in solution through surface modification with conducting polymers, metals, and oxides [5–7]. These protective layers not only inhibit photo-corrosion of Cu<sub>2</sub>O, but also facilitate the band structure for improved charge transport [6]. Despite the highlighted issue, Cu<sub>2</sub>O remains a thoroughly researched semiconductor material due mainly to the distinct qualities and characteristics that set it apart. Cu<sub>2</sub>O has a narrow band gap

(1.8–2.5 eV) as compared to other semiconductor oxides [7], a high abundance in the earth's crust, and can be synthesized via a variety of processes that are both low-cost and scalable. When dealing with nanostructured  $\text{Cu}_2\text{O}$ , the electrochemical and chemical stability, band gap level, flat band potential, and even the nature of semi-conductivity can vary considerably depending on the synthesis method used to produce them [8,9]. The ability to precisely control these qualities of  $\text{Cu}_2\text{O}$  leads to a number of new and exciting applications. One of the most extensively investigated applications is the  $\text{Cu}_2\text{O}$ -catalysed, light-driven purification of wastewater [10]. For example, various combinations of metal- $\text{Cu}_2\text{O}$  nanoparticles have been used for the decontamination of water polluted with dyes or hydrogen peroxide [11]. Here,  $\text{Cu}_2\text{O}$  particles are labeled cleaning “nano-swimmers” or “micromotors” as they exhibit self-propelled movement, driven by gases that are generated at one end of the  $\text{Cu}_2\text{O}$  particle. With this  $\text{Cu}_2\text{O}$ -based decontamination method, new cleaning suspensions represent a less toxic alternative when compared to conventional water purification methods that produce enormous quantities of secondary waste (e.g., chromium, iron compounds).

Another important application of  $\text{Cu}_2\text{O}$  is to catalyze organic coupling reactions, including carbon–carbon [12], and nitrogen–carbon couplings [13].  $\text{Cu}_2\text{O}$ -catalyzed synthesis (with and without illumination) of amides via amidation of aryl halides [14], Sonogashira- [15], and Suzuki-type couplings [16,17], have shown excellent conversion with satisfactory yields under mild reaction conditions at much lower cost (as compared to palladium-catalyzed syntheses). Moreover, a recyclable  $\text{Cu}_2\text{O}$  nano-catalyst has been utilized for nitrogen–carbon cross coupling of aryl halides with aromatic/aliphatic amides [18] and amines [13], as well as numerous types of  $\text{Cu}_2\text{O}$ -driven cycloaddition reactions (e.g., click chemistry [19], Huisgen cycloaddition [20]). The good selectivity and low toxicity, together with excellent yields of the  $\text{Cu}_2\text{O}$ -catalyzed methods, make this an inexpensive catalyst that is especially important for up-scaled production.

Likewise,  $\text{Cu}_2\text{O}$  in combination with other oxides or metals has been reported as a very promising catalyst in the light-driven conversion of  $\text{CO}_2$  to fuels and feedstocks [21,22]. For example, Cu- $\text{Cu}_2\text{O}$  and Cu- $\text{Cu}_2\text{O}$ -ZnO have shown excellent activity towards electrochemical reduction of  $\text{CO}_2$  to higher alcohols, with the Cu- $\text{Cu}_2\text{O}$ -ZnO catalyst being the most selective for methanol generation [23]. With sustainable solar energy as a resource, photocatalytic reduction of  $\text{CO}_2$  is in high demand for the production of technologically important gaseous and liquid chemicals, such as methane and methanol. More importantly,  $\text{Cu}_2\text{O}$ -catalyzed conversion of  $\text{CO}_2$  has enormous potential for use in the reduction of greenhouse gases, which may assist in minimizing one source of climate change.

In previous studies,  $\text{Cu}_2\text{O}$  has been synthesized through various chemical [24,25], electrochemical [26,27], and mechanochemical pathways [28,29]. Although these methods resulted in  $\text{Cu}_2\text{O}$  with new structures and photocatalytic efficiencies, many of them pose potential environmental risks as they require hazardous reactants (e.g., sodium hydroxide) or metal precursors (e.g., copper nitrite, copper chloride, copper sulfate), and often generate a high volume of by-product [30]. Thus, a synthesis method that is capable of producing mass amounts of  $\text{Cu}_2\text{O}$  in a fashion that is both environmentally friendly and relatively inexpensive is of great interest to researchers. One of the most promising techniques in this regard is electrochemical synthesis. This is due to its ability to generate copper ions directly from metals, without the use of additional chemicals. Other benefits of  $\text{Cu}_2\text{O}$  electro-synthesis include the ability to control the rate of reaction, the simplicity of the setup, the ease with which the reaction can be scaled up, and the generation of highly porous  $\text{Cu}_2\text{O}$  nanostructures [31]. As an example,  $\text{Cu}_2\text{O}$  was previously synthesized using a closed bipolar electrochemical setup that utilized four electrodes and  $\text{CuSO}_4$  as the source of copper ions, and was pioneered by Ugo et al. in 2016 [32]. This work demonstrated that porous  $\text{Cu}_2\text{O}$  deposit can be synthesized simultaneously with metal or metal oxides in one electrochemical reactor, and was used to generate unique structures called Janus particles.

One electrochemical method that has never been utilized in the large-scale production of  $\text{Cu}_2\text{O}$  is a wireless electro-synthesis process known as open bipolar electrochemistry (BPE).

BPE is a contactless method and consists of a conductive object (BPE electrode) that is placed between two driving electrodes. This BPE electrode develops opposite charges at each end, hence the

name bipolar, and can thus facilitate oxidation and reduction reactions simultaneously [33]. Redox reactions in solution are driven forward by overpotentials that form on the extremities of the wireless electrode. The potential difference between two redox reactions occurring at the bipolar electrode,  $\Delta E_{\text{elec}}$ , is determined by the equation:

$$\Delta E_{\text{elec}} = E_{\text{tot}} \left( \frac{l_{\text{elec}}}{l_{\text{channel}}} \right) \quad (1)$$

where  $E_{\text{tot}}$  represents the total applied potential;  $l_{\text{channel}}$  is the distance between the two driving electrodes; and  $l_{\text{elec}}$  is the thickness of the bipolar electrode. When a sufficient potential is applied to the cell, oxidation of the copper plate, paired with the reduction of water, takes place on the wireless and driving electrodes, respectively (Figure S1). In the proposed BPE synthesis, the formation of  $\text{Cu}_2\text{O}$  species is only possible in the presence of potassium gluconate, which has multiple roles: as an electrolyte (to increase the conductivity of the solution); as a complexing agent ( $\text{C}_{12}\text{H}_{22}\text{CuO}_{14}$ ); and, most importantly, as a reducing agent, allowing for the generation of  $\text{Cu}^+$  ions. Potassium gluconate is a low-cost food supplement and assists several functions of the body (e.g., it is used to regulate potassium levels in the blood [34]). Herein, we exploit the gluconate as an essential reactant in the synthesis of nanostructured  $\text{Cu}_2\text{O}$ . This allows for the removal of more harmful reducing agents required in other  $\text{Cu}_2\text{O}$  syntheses. In addition, one of the most important benefits of BPE is the ability to exclude corrosive reactants, such as hydroxide, that are used in conventional  $\text{Cu}_2\text{O}$  fabrication. In the BPE process, the hydroxide species are generated in situ via water electrolysis occurring at the driving electrodes (Equation (S2), Figure S1). The formation of  $\text{Cu}^{2+}$  on the bipolar electrode, accompanied by the production of stoichiometric amounts of  $\text{OH}^-$  on the driving electrode, is controlled by a low applied potential so that no excess of corrosive by-product is generated. In this work, a series of nanostructured  $\text{Cu}_2\text{O}$  have been synthesized in the BPE reactor. The effect of applied voltage and reaction time on structure and photo-electrochemical characteristics are explored and compared to commercial  $\text{Cu}_2\text{O}$ . The BPE approach is highly scalable, easy to control, and can open new avenues in the industrial production of various nanostructured materials, as it is both cost effective and safer for the environment.

## 2. Materials and Methods

### 2.1. Materials

Potassium D-gluconate ( $\geq 99\%$ , CAS# 299-27-4), fluorine-doped tin oxide (FTO) plates ( $300 \times 399 \times 2.2$  mm resistivity  $7 \Omega/\text{cm}^2$ ), and cuprous oxide ( $\geq 99.99\%$ , trace metal basis, CAS# 1317-39-1) were purchased from Sigma-Aldrich (Oakville, ON, Canada). Anhydrous ethanol (100%, CAS# 64-17-5) was obtained from Commercial Alcohols and sodium sulfate ( $>99\%$ , CAS# 7757-82-6) was obtained from Fisher Scientific (Nepean, ON, Canada).

### 2.2. Characterization

#### 2.2.1. X-Ray Diffraction (XRD)

The composition and crystalline structure of cuprous oxide samples was investigated using XRD. All XRD analyses were performed using a Bruker AXS D8 microdiffractometer (Bruker Corp., Billerica, MA, USA) with a  $\text{Cu-K}\alpha$  X-ray tube, a wavelength ( $\lambda$ ) of  $1.54 \text{ \AA}$ , and an accelerating voltage of 40 kV. All samples were prepared in a circular well and levelled off to ensure a smooth surface for analysis.

#### 2.2.2. X-Ray Photoelectron Spectroscopy (XPS)

XPS analysis was performed to measure the elemental composition of the prepared and commercial cuprous oxide samples. XPS measurements were obtained using a VG Microtech MultiLab ESCA 2000

spectrometer (VG Microtech Limited, London, UK) with 100  $\mu\text{m}$  analyzer spatial resolution, 10 meV energy resolution, and Mg  $K\alpha$  linewidth.

### 2.2.3. Transmission Electron/Scanning Electron Microscopy (TEM/SEM)

The morphology of cuprous oxide samples was investigated using TEM and SEM at Friedrich-Schiller University (FSU) and the University of New Brunswick (UNB). A suspension of  $\text{Cu}_2\text{O}$  (0.5 mg/mL) was deposited onto a nickel grid (TEM) or ultra-smooth glassy background (SEM). A JEOL JSM-6400 SEM (Jeol Ltd., Tokyo, Japan), equipped with an EDAX Genesis 4000 energy dispersive X-Ray (EDX) analyzer, was used at an accelerating voltage of 15 kV (UNB). High resolution TEM (HRTEM) was carried out with a JEOL 3010 and JEOL NeoARM TEM (Jeol Ltd., Tokyo, Japan).

### 2.2.4. UV-Vis Diffusive Reflectance

UV-Vis diffusive reflectance studies were performed using a Lambda 25 UV/VIS spectrometer double beam (DB) instrument (PerkinElmer Inc., Waltham, MA, USA) in the wavelength range from 200 to 1200 nm.

### 2.2.5. Photoluminescence

Emission measurements were carried out using thin film  $\text{Cu}_2\text{O}$ . For thin film preparation, a paste of 1 mg/1 mL (MeOH) was drop-cast on a  $2 \times 1$  cm masked glass substrate and dried at 90 °C for 1 h (low temperature drying was used to avoid microstructure alteration).

The apparatus used was a FLS980 spectrometer (Edinburgh Instruments, 2 Bain Square Kirkton Campus, UK). A NIR PMT detector was used for wavelength scans beyond 850 nm.

### 2.2.6. Electrochemical Characterization

All electrochemical experiments were conducted using a three-electrode system with a  $\text{Cu}_2\text{O}$ |FTO plate working electrode, a platinum wire counter electrode, and an Ag/AgCl (saturated KCl,  $E = 0.197$  V) reference electrode in 0.5 M sodium sulfate. A CHI 660-E potentiostat (CH Instruments Inc., USA) was used for all electrochemical tests. Photocurrent was analyzed under open circuit potential (OCP) by subjecting the working electrode to intermittent illumination in fifty second intervals using an 85 W Xe Sunworld HID light source. Mott-Schottky (MS) analysis was performed under a reverse bias from 0.1 to 0.6 V at 10 kHz, with a potential step of 0.05 V. The voltage range for MS and photocurrent tests was determined by cyclic voltammetry (CV). The potential range with no copper redox activity was used for MS analysis. AC impedance was carried out, without applied bias, under dark and illuminated conditions and in a frequency range of  $10^{-2}$ – $10^5$  Hz.

### 2.2.7. Fabrication of $\text{Cu}_2\text{O}$ Electrode

Prior to the casting of  $\text{Cu}_2\text{O}$ , FTO glass plates were cleaned in acetone and ethanol by ultrasonication, and then washed with deionized (DI) water. 10 mg of  $\text{Cu}_2\text{O}$  in 5 mL of anhydrous ethanol was sonicated for 1 h. Finally, 125  $\mu\text{L}$  of  $\text{Cu}_2\text{O}$  suspension was deposited onto the FTO plate and allowed to dry at ambient conditions (the area of electrode was 1  $\text{cm}^2$  for all samples).

### 2.2.8. Synthesis Procedure

Potassium gluconate solution was used as both an electrolyte and complexing agent for the free copper ions released during the BPE process from the Cu plate. 4.5 g of potassium gluconate was dissolved in one litre of pure DI water (19.2 mM) reaching pH = 6.8. 200 mL of the potassium gluconate solution was heated to 80 °C. A copper plate and driving electrodes were secured in a custom-made Teflon top. A constant potential was applied for 1 h at 4.5, 5.0, 6.0, 7.0, and 8.0 V, or for 3 h at 4.5 V, as presented in Figure S1. The precipitate was filtered, washed three times with distilled water and then with ethanol, dried, and stored in ambient conditions. A reaction mixture was sampled at time



intervals to demonstrate the various stages of the reaction for the  $\text{Cu}_2\text{O}$  synthesized at 6.0 V (Figure S2). At 0 min, the solution consisted of a copper plate that was immersed in 19.2 mM potassium gluconate solution. The applied potential resulted in the oxidation of the copper plate (Figure S1, Equation (S1)), which was paired with the reduction of water (Equation (S2)). At 5 min, a dilute concentration of copper gluconate had formed (Equation (S3)), which was demonstrated by the slight blue color of the solution. This converted into a green tint by 10 min due to the generation of copper (I) hydroxide ( $\text{CuOH}$ ). The  $\text{CuOH}$  formed due to the reduction of the  $\text{Cu}^{2+}$  by glucose (Equation (S4)) and the subsequent reaction with free hydroxide ions (Equation (S5)). As the concentration of  $\text{CuOH}$  increased, and  $\text{Cu}_2\text{O}$  was subsequently generated by degradation of  $\text{CuOH}$  (Equation (S6)), the solution color changed to yellow over 20 min (Figure S2). Finally, due to the increased concentration and the size of the  $\text{Cu}_2\text{O}$  particles, the colour of the suspension darkened to orange. All samples exhibited the same steps in the synthesis process; however, the color changes occurred faster as the synthesis potential increased. The reaction steps are shown in Figure S2 in both sampled solution (top photos) and in the BPE electrochemical cell (bottom photos).

### 3. Results

#### 3.1. Structural Analysis of $\text{Cu}_2\text{O}$

The effects of varying potential and time on the structure of as-synthesized  $\text{Cu}_2\text{O}$  was investigated using X-ray diffraction (XRD), followed by a Rietveld refinement analysis. Initial observations indicated that all synthesized material was phase-pure due to the absence of metallic copper and  $\text{CuO}$ . As represented in Figure 1,  $\text{Cu}_2\text{O}$  samples exhibited the most intense XRD peak at approximately  $36.5^\circ 2\theta$ , indicating preferred growth towards a 111 orientation. All BPE-generated oxides showed much broader XRD patterns and, thus, had smaller crystallite sizes compared to the commercial  $\text{Cu}_2\text{O}$ . In addition, referring to the commercial  $\text{Cu}_2\text{O}$ , a slight shift was observed towards higher values of  $2\theta$  for all BPE-synthesized samples (Figure 1a–c). These shifts in BPE-synthesized oxide were assumed to be caused by either stress-strain or structural defects in the lattice.

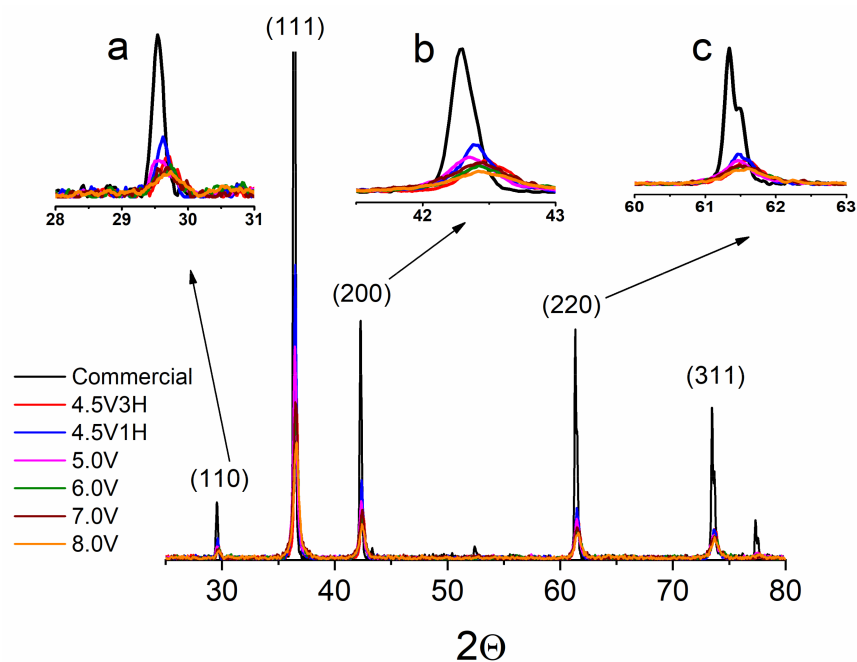


**Figure 1.** X-ray diffraction patterns of commercial  $\text{Cu}_2\text{O}$  (black) and  $\text{Cu}_2\text{O}$  synthesized by bipolar electrochemistry at different applied voltages and synthesis times. The reference signals are assigned to cubic  $\text{Cu}_2\text{O}$  according to JCPDS (The Joint Committee on Powder Diffraction Standards) card number 00-005-0667. Inserts a, b, and c are enlarged patterns (110), (200) and (220), respectively.

Both crystallite size and lattice constants are presented in Table 1. The particle size was calculated using Scherrer's equation [35] (Equation (2)), where  $D$  is the crystallite size in nm,  $\lambda$  is the Cu  $K\alpha$  radiation wavelength (1.5046 Å),  $K$  is the shape factor (0.9),  $\beta_{hkl}$  is the full width at half maximum (FWHM) in radians, and  $\theta$  is the scattering angle in radians.

$$D = \frac{K\lambda}{\beta_{hkl}\cos\theta} \quad (2)$$

**Table 1.** Refinement data collected from the Rietveld analysis of room temperature XRD data for BPE-synthesized  $\text{Cu}_2\text{O}$ . All samples showed very good correlation with the  $\text{Cu}_2\text{O}$  model (space group:  $Pn-3m$ , with atom positions for Cu of (0,0,0) and O of ( $\frac{1}{4}, \frac{1}{4}, \frac{1}{4}$ )). Parameter  $\chi^2$  is goodness-of-fit,  $R_{wp}$  is weighted profile,  $R_p$  is profile residual, and  $a$  is the lattice parameter in Angstroms (Å). Crystallite size was calculated from the Scherrer formula (Equation (2)).

Parameter	4.5 V-3H	4.5 V-1H	5.0 V	6.0 V	7.0 V	8.0 V
$\chi^2$	1.17	1.32	1.31	1.33	1.42	1.29
$R_{wp}$ (%)	10.84	10.03	9.94	10.46	10.14	10.42
$R_p$ (%)	8.51	7.95	7.79	8.01	7.93	8.07
$a$ (Å)	4.26	4.26	4.27	4.26	4.26	4.26
Cell Vol (Å <sup>3</sup> )	77.53	77.53	77.69	77.36	77.42	77.43
Cu-O bond length (Å)	1.85	1.85	1.85	1.84	1.84	1.84
Cu-O-Cu bond angle (°)	109.47	109.47	109.47	109.47	109.47	109.47
Crystallite size (nm)	27.1	21.7	20.3	16.2	15.6	14.5

As seen in Table 1, crystallite size decreased as the applied potential in the BPE synthesis increased, with a minimum (14.5 nm) occurring at the maximum applied potential of 8.0 V. Similarly, by extending the reaction time from 1 to 3 h (sample synthesized at 4.5 V, red and blue patterns in Figure 1), crystallite size increased from 21.7 to 27.1 nm. Thus, using BPE to synthesize  $\text{Cu}_2\text{O}$ , crystallite size can be decreased by either increasing the applied voltage or decreasing the synthesis duration.

Rietveld analysis (Figures S3–S8) was performed for the diffraction data collected for all materials using the GSAS software [36,37] and the model for  $\text{Cu}_2\text{O}$  proposed by Foo et al. (as taken from the ICSD) [38]. Refinements were performed for twenty variables, which included lattice parameters, atom positions, zero-point, peak shape, and background. The background was modelled with twelve terms via a shifted Chebyshev polynomial function. The peak shape was modelled using the pseudo-Voigt function, as described by Howard and Thompson et al. [39,40]. To mitigate surface roughness effects that were introduced by preparation of the sample for X-ray diffraction analysis, six spherical harmonic order terms were also refined in a cylindrical geometry. In all cases, the texture index was close to 1, indicating that the sample was randomly oriented. Refinement data is included in Table 1, with the refinement profiles given in Figures S3–S8. All materials showed an excellent fit to the proposed model. The lattice parameters, as listed in Table 1, demonstrated no significant impact on lattice structure or Cu–O bond lengths when either applied potential in BPE synthesis or reaction time were altered. However, as previously discussed, increasing applied potential did allow for a decrease in the overall crystallite size. Therefore, apart from crystallite size, it is assumed that time and potential played no further role in augmenting the presented samples.

Photoluminescence (PL) analysis was carried out at various excitation wavelengths on all  $\text{Cu}_2\text{O}$  samples. PL data (Figures S9–S13) confirmed an insignificant amount of structural defects in all BPE-synthesized and commercial samples through the lack of oxygen and copper vacancy peaks, which typically appear around 700–750 nm and 910–920 nm, respectively [41]. This apparent absence of structural defects suggests that any shifts in the XRD patterns of as-synthesized  $\text{Cu}_2\text{O}$  are the result of lattice strain.

### 3.2. Morphology

Figure 2a–d presents SEM images of Cu<sub>2</sub>O synthesized at 4.5 V-1H, 6.0, 7.0, and 8.0 V. Agglomeration for all samples was significant despite several attempts to improve dispersal using surfactants (PVP, SDS, CTAB, Triton X-100, HMT); thus, individual structure determination was impossible. All images presented show samples without added surfactants. SEM observations further demonstrated that Cu<sub>2</sub>O agglomerates were porous and composed of much smaller structures.

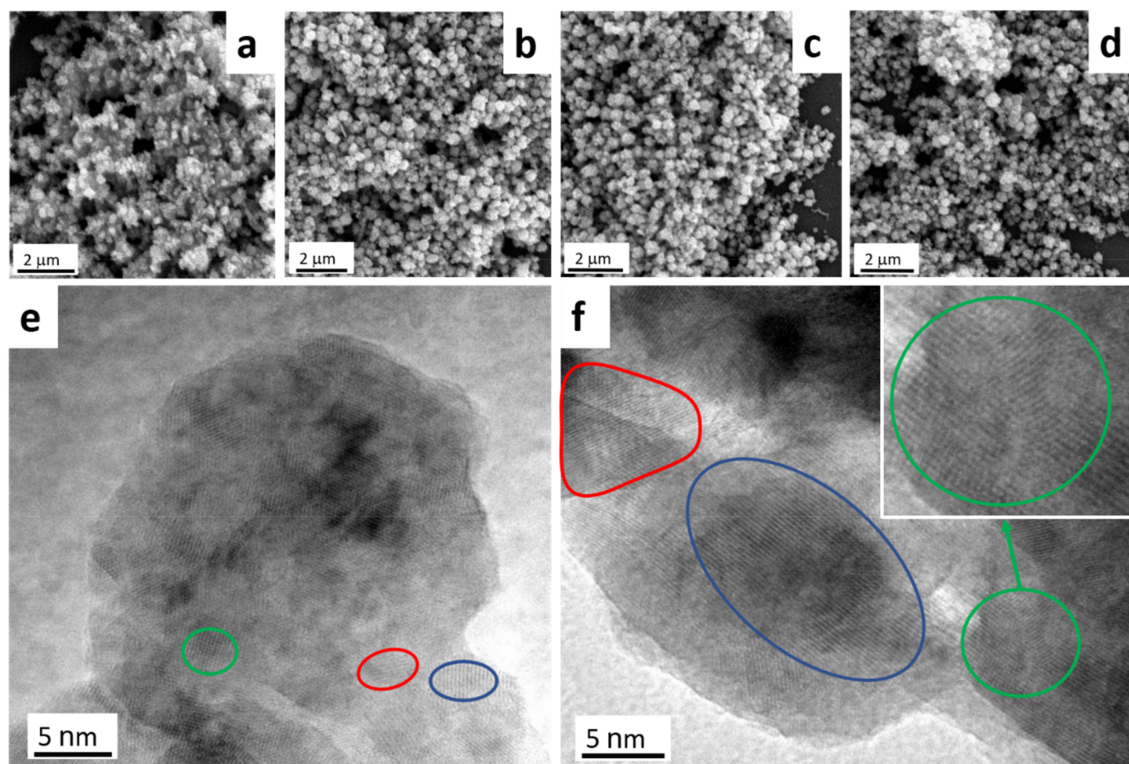


**Figure 2.** SEM images of 4.5 V-1H, 6.0, 7.0, and 8.0 V Cu<sub>2</sub>O samples (a–d, respectively) and HRTEM images of 4.5 V-1H (e) and 7.0 V (f) samples.

HRTEM images of 4.5 V-1H and 7.0 V samples are shown in Figure 2e,f, respectively. The individual size of particles revealed by TEM agree well with the crystallite size calculated from XRD data (Table 1). Crystallites imaged through TEM contain several different substructures (Figure 2, red and blue circles) composed of similarly oriented lattice planes. Substructures in the 4.5 V-1H sample were much smaller than those in the 7.0 V sample, suggesting a higher variability in lattice orientation with lower applied voltages. The green circles in Figure 2e,f highlight areas of changing lattice orientation and contain two or more overlapped substructures.

While the Rietveld analysis of BPE-synthesized Cu<sub>2</sub>O suggested no significant difference in particle shape with varying synthesis times and potentials, TEM/SEM of commercial Cu<sub>2</sub>O revealed considerable differences between the as-synthesized and commercial products (Figures S14–S15). The commercial material showed much larger and more irregular agglomerates that were bigger than 1 μm. The crystallite size for the reference material, calculated by Equation (2), was also much larger (92.9 nm) than oxides produced in this work. Therefore, the proposed bipolar electrosynthesis can produce nano-sized Cu<sub>2</sub>O particles that are both phase-pure and defect-free.

### 3.3. X-Ray Photoelectron Spectroscopy (XPS): Surface Chemistry

Figure 3a shows an example of the O 1s signal for BPE-made Cu<sub>2</sub>O (6.0 V). Signal deconvolution reveals two main components: the peak at 531.4 eV represents the O–Cu(+1) in Cu<sub>2</sub>O, and the larger

peak at 532.0 eV generally represents  $\text{Cu}_2\text{O}$ ,  $\text{Cu}(\text{OH})_2$ , and/or  $\text{CuO}$ . Since deconvolution of the  $\text{Cu } 2p_{3/2}$  signal (Figure 3b) identified  $\text{Cu}(+1)$  as the main signal, the  $\text{O } 1s$  peak at 532.0 eV represents either a defective oxygen lattice in  $\text{Cu}_2\text{O}$  (not identified in the BPE-synthesized  $\text{Cu}_2\text{O}$  based on photoemission analysis, Figures S9–S13), or the presence of adsorbed oxygen from water or carbonates [42]. As shown in Figure 3b, the main  $\text{Cu}_2\text{O}$  peak was observed at 932.4 eV, with a weak  $\text{Cu}(\text{II})$  signal appearing at 935.2 eV. This weak  $\text{Cu}(\text{II})$  peak may be the result of minor surface oxidation due to long-term air exposure or the presence of  $\text{Cu}(\text{OH})_2$  residue formed during the synthesis [40]. Regardless of this impurity, XRD analysis of product stored in ambient conditions for an extended time identified  $\text{Cu}_2\text{O}$  as the only phase. Furthermore, the  $\text{Cu } 2p_{3/2}$  signal (Figure 3b) confirmed the absence of both metallic copper and  $\text{CuO}$ , validating that the material was phase-pure. The  $\text{Cu}$  LMM peak identified at 952.3 eV (Figure 3b) corresponds to  $\text{Cu}_2\text{O}$  [43,44]. Figure 3c compares the  $\text{O } 1s$  signals for all  $\text{Cu}_2\text{O}$  samples. Signals for as-synthesized oxides are slightly shifted towards lower binding energies, with the 4.5 V-3H sample peak nearly matching the commercial sample.

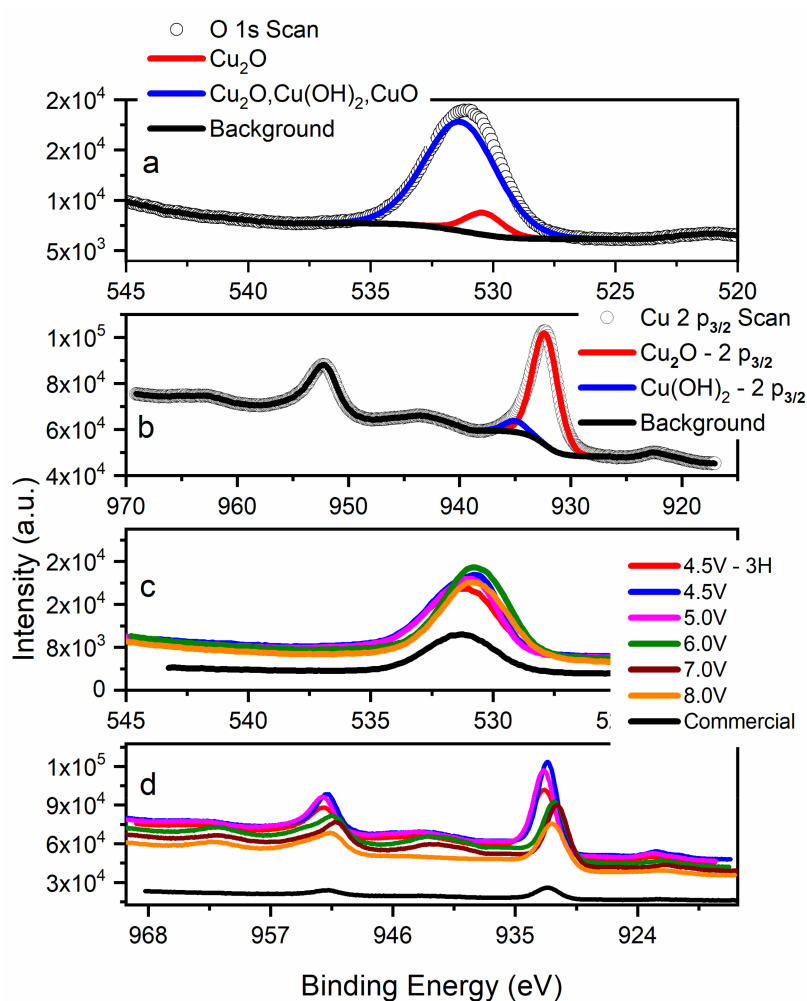


**Figure 3.** X-ray photoelectron spectroscopy of  $\text{O } 1s$  (a) and  $\text{Cu } 2p$  (b) signals for the 6 V sample; and overlay of  $\text{O } 1s$  (c) and  $\text{Cu } 2p$  (d) spectra for the commercial (black) sample and samples synthesized by bipolar electrochemistry at different applied voltages and times.

Despite shifts in the  $\text{Cu } 2p_{3/2}$  peaks (Figure 3d), no trend related to the applied synthesis voltage was observed. These chemical shifts could be related to several factors, including lattice strain, surface oxygen defects, or differences in particle size. An important observation is that  $\text{Cu}_2\text{O}$  generated at 8.0 V showed no signs of degradation through the absence of  $\text{Cu } 2p_{3/2}$  satellite peaks ( $\sim 943.0$  eV), unlike the 6.0 and 7.0 V samples (Figure 3d).

### 3.4. Optical Studies: Diffusive-Reflectance UV–Vis and Kubelka–Munk Analysis

The diffusive reflectance spectra of the commercial and BPE-synthesized samples are presented in Figure 4a. As-prepared oxides showed better light absorption than the commercial material in the range from 200–420 nm. This increase in absorption is best explained by the higher concentration per unit area (higher surface area) of nanometer-sized oxides made in this work when compared to the reference material. Cu<sub>2</sub>O prepared by the BPE method demonstrated a gradual increase in reflectance, starting at approximately 450 nm (all samples). In contrast, the % reflectance of the commercial Cu<sub>2</sub>O showed a sharp increase around 600 nm. This difference can be explained by the effect of particle size—decreasing the particle size induced an increase in the band gap of the material, which altered the ideal absorption wavelength (i.e., blue shifting nanomaterial). The band gap energies were determined by applying the Kubelka–Munk function:

$$F(R) = \frac{K}{S} = \frac{1 - R_{\infty}}{2R_{\infty}} \quad (3)$$

where  $R$  is the absolute value of reflectance,  $F(R)$  is the absorption coefficient equivalent,  $K$  is the absorption coefficient,  $S$  is the scattering coefficient, and  $R_{\infty}$  is the diffusive reflectance of the film. A Tauc plot (Figure 4b) correlates the Kubelka–Munk function and energy of a photon,  $(F(R) \times E_{\text{photon}})^2 = f(E_{\text{photon}})$ , enabling extrapolation of the band gap energy. For the commercial material, the band gap energy is close to values reported in the literature ( $\sim 2$  eV) [45]. Interestingly, Cu<sub>2</sub>O prepared via BPE exhibited a higher band gap energy of approximately 2.5 eV for all samples. This increase in energy is caused by the quantum confinement effect, which is the generation of discrete energy levels in the valance and conduction bands. This, in turn, results in an increase in the band gap and is often observed in nano-sized materials [46,47]. The optical analysis revealed two competing effects: Higher band gap energies in BPE-made Cu<sub>2</sub>O due to its smaller particle size (possibly due to the presence of substructures), and an increased light absorption below 450 nm, as compared to the reference material. This demonstrates that the nano-sized Cu<sub>2</sub>O prepared by BPE may scavenge light more efficiently when compared to the commercial sample.

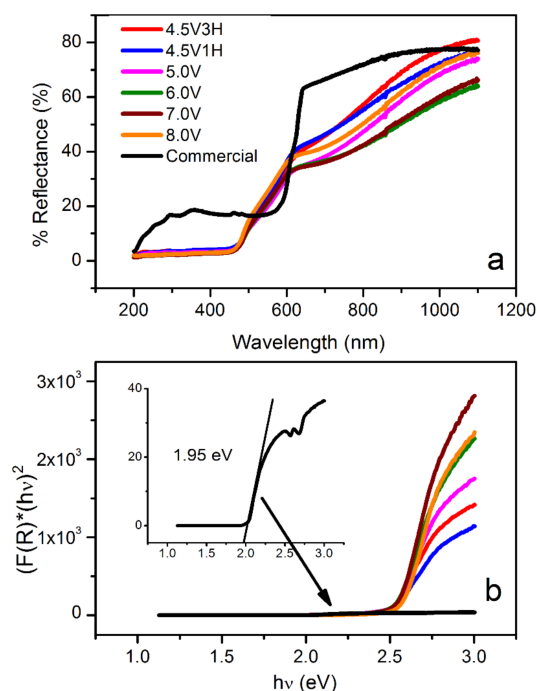


**Figure 4.** UV–Vis diffusive reflectance spectra (a) and Kubelka–Munk function versus bandgap energy (b) for commercial Cu<sub>2</sub>O (black) and Cu<sub>2</sub>O synthesized by bipolar electrochemistry at different applied voltages and times.



### 3.5. Mott–Schottky Analysis: Flat-Band Potential and Carrier Concentration

Mott–Schottky (MS) analysis resulted in estimation of the flat band potential ( $E_{fb}$ ), charge carrier concentration, and type of semi-conductivity [48]. The space-charge capacitance was determined from the imaginary section of the impedance. MS plots are presented in Figure 5a for all samples, including the commercial oxide. Both the reference and synthesized  $\text{Cu}_2\text{O}$  demonstrated a negative slope for the MS function, which indicated a p-type semi-conductivity. For p-type semiconductors, the majority of carriers are electron holes and the carrier concentration can be determined by Equation (4).

$$\frac{1}{C^2} = \left( \frac{2}{\epsilon\epsilon_0 * N_a^2} \right) \left( V - V_{fb} - \frac{kT}{e} \right) \quad (4)$$

where  $e$  is the elementary charge of an electron,  $N_A$  is the acceptor density,  $\epsilon$  is the dielectric constant of  $\text{Cu}_2\text{O}$  (7.26),  $\epsilon_0$  is the permittivity of free space,  $T$  is the temperature in K, and  $k$  is Boltzmann's constant. The flat band potential ( $V_{fb}$ ) and carrier concentration are estimated by extrapolating the linear region of the MS function to determine the x-intercept and utilizing the slope in Equation (5), respectively.

$$\text{Slope} = \left( \frac{2}{\epsilon\epsilon_0 N_a^2} \right) \quad (5)$$

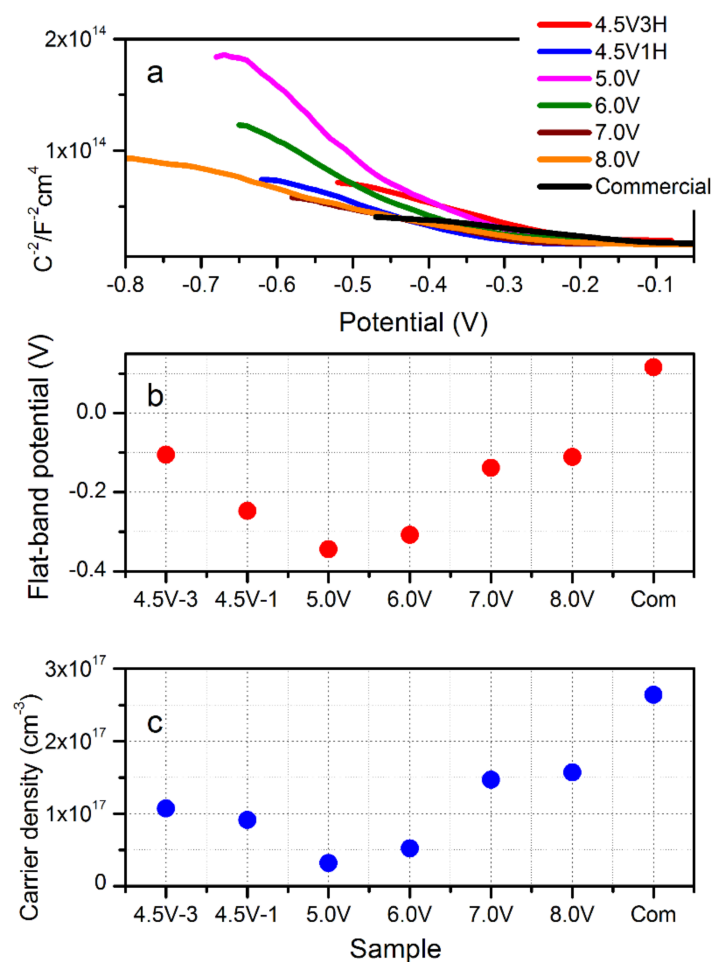


**Figure 5.** Mott–Schottky (MS) plots (a); flat-band potential estimated from linear fit of MS plot (b); and carrier density (c) calculated from Equations (4) and (5).

The flat band potential and carrier concentration are shown in Figure 5b,c. As the flat band potential increased, the carrier concentration increased as well. The effect of applied voltage in the BPE



synthesis was observed above 5.0 V. 8.0 V had the largest flat band potential and carrier concentration at  $-0.11$  V and  $1.57 \times 10^{17} \text{ cm}^{-3}$ , respectively, which represents an overall increase of 0.136 V across the BPE potential range. The synthesis time for materials synthesized at 4.5 V had almost no influence on carrier density. A slightly lower flat band potential was observed for  $\text{Cu}_2\text{O}$  made at extended time (3 h). It can be assumed that for the BPE-synthesized  $\text{Cu}_2\text{O}$ , the differences in both  $V_{\text{fb}}$  and  $N_{\text{a}}$  are strongly related to structural changes and surface chemistry, as demonstrated by XRD and XPS. Moreover, the presence of ultra-fine substructures within the particle—the nature of the grain boundaries—may explain the observed trends in  $V_{\text{fb}}$  and  $N_{\text{a}}$ . On the other hand, the commercial oxide had a higher  $V_{\text{fb}}$  and  $N_{\text{a}}$  than all  $\text{Cu}_2\text{O}$  synthesized in this work. This effect is caused by the increased crystallinity of the reference  $\text{Cu}_2\text{O}$  as compared to particles on the nanoscale.

### 3.6. Photo-Electrochemistry: Carrier Lifetime and Photocurrent

Analysis of Bode-phase plots (Figure 6a) was exploited to calculate the charge recombination time in dark and illuminated conditions. By evaluating the maximum peak frequency, the recombination times can be calculated using Equation (6).

$$\tau = \frac{1}{2\pi f_{\text{max}}} \quad (6)$$

where  $\tau$  is the carrier lifetime and  $f_{\text{max}}$  is the maximum frequency. Figure 6b depicts the calculated carrier lifetimes, with 4.5 V-3H having the longest lifetime at 38 ms. Significantly shorter lifetimes (two orders of magnitude shorter) were observed for  $\text{Cu}_2\text{O}$  made at higher voltages. Comparatively, the reference sample showed a carrier lifetime within the range of those synthesized by BPE, except for samples made at 4.5 V. The significant increase in carrier lifetime for the 4.5 V-3H is beneficial for photocatalysis due to a reduced rate of electron-hole recombination that allows electrons to participate in photocurrent generation. In total, this analysis led to the conclusion that the charge recombination rate varied for samples synthesized at different times (4.5 V-1H and 4.5 V-3H), but was not influenced by the applied synthesis voltage.

Photocurrent density was determined using an  $I-t$  (current-time) curve under open circuit potential (OCP) and intermittent illumination. As demonstrated in Figure 7, for  $\text{Cu}_2\text{O}$  synthesized at higher potentials and longer reaction times, an increase in photocurrent was observed. This is likely due to the difference in structure/morphology (in particular, the particle size effect and the presence of ultra-fine substructures), resulting in various grain boundaries [49], as demonstrated by TEM imaging. The trend observed can be further correlated with the increase in carrier concentration and flat band potential, as demonstrated in Figure 5b,c. The higher carrier concentration and flat band potential are related to smaller particle size (for samples that were synthesized at higher BPE voltage). These two factors allowed for improved total current generation by introducing greater band bending. This contributed to a better charge separation, while simultaneously increasing the concentration of separated charges [48]. Furthermore, the increase in the carrier lifetime for  $\text{Cu}_2\text{O}$  synthesized at 4.5 V-3H allowed for a larger photocurrent due to better transfer of the carriers. This increase was expected due to better crystallinity, which is closer to that of the commercial  $\text{Cu}_2\text{O}$ . However, as indicated by the initial sharp peak (Figure 7), transient current peaks appeared upon illumination across all samples that were synthesized via BPE. Transient peaks occurred due to a large degree of surface electron recombination [50,51]. Carriers that are generated in the space charge region are accelerated towards the semiconductor-electrolyte junction, which builds up until the rate of water redox reactions are balanced with the arrival of the carriers. The large surface recombination then reduces the photocurrent that is generated by  $\text{Cu}_2\text{O}$  due to inefficient carrier extraction. This effect weakens for  $\text{Cu}_2\text{O}$  that is synthesized at higher voltages. Presumably, a more efficient charge transfer occurs for smaller particles that have larger surface contact with the electrolyte. This effect can be further influenced by combining oxides with more conductive additives for better photo-carrier harvesting [51]. Lastly, the commercial material demonstrated a significant decrease in photocurrent with respect to the

synthesized samples. This effect is likely caused by the decreased photoabsorbance of the material resulting in a negative impact on the photogenerated carriers. Therefore, as the synthesized material has significantly higher photocarrier generation, the photocurrent is expected to increase.

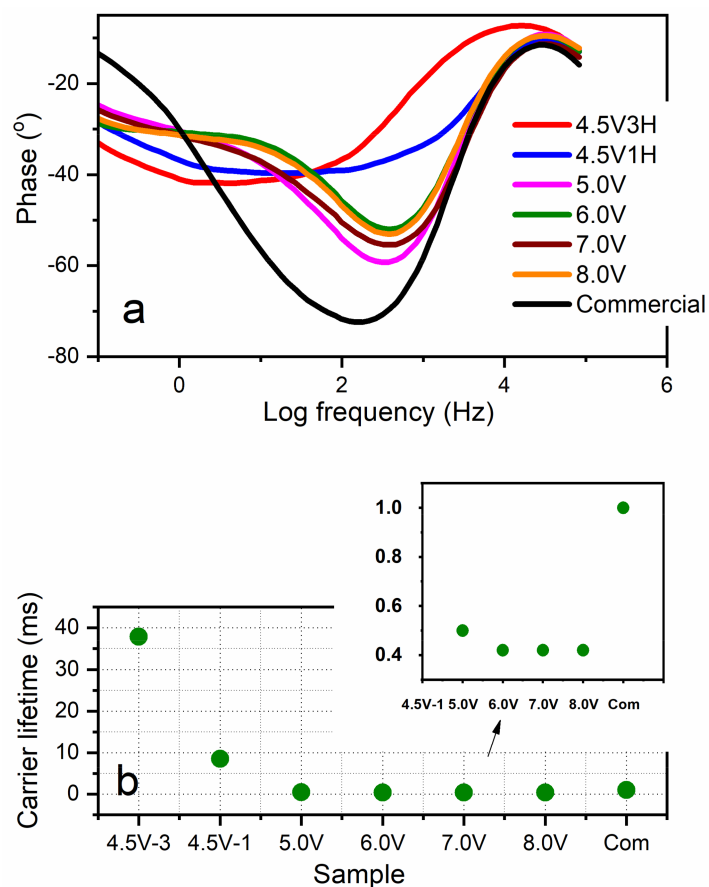


**Figure 6.** Bode plots for illuminated Cu<sub>2</sub>O electrodes synthesized by bipolar electrochemistry and for commercial Cu<sub>2</sub>O (a); carrier lifetime calculated from Equation (6) (b).

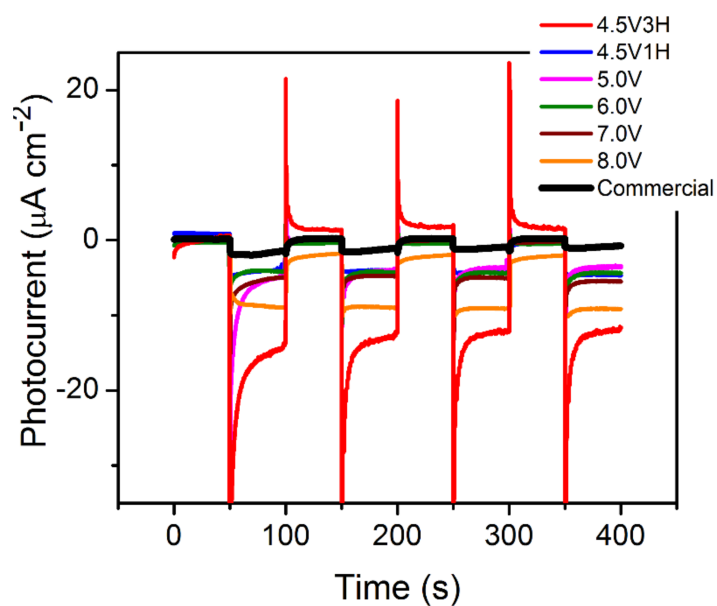


**Figure 7.** Photo-current density response of Cu<sub>2</sub>O electrodes with illumination intervals of 50 s.

#### 4. Conclusions

We demonstrate a wireless bipolar electrochemical synthesis of cuprous oxide, targeting the impact of reaction conditions (applied potential and reaction time) on structure, morphology, surface chemistry, and photo-electrochemical activity. SEM/TEM imaging revealed porous-agglomerated materials composed of ultra-fine substructures (2–5 nm) within a single particle in oxide synthesized at low potentials. UV–Vis studies and Kubelka–Munk analysis demonstrated that there was no significant shift in wavelength absorbance/band gap across the synthesized samples. Referring to commercial material, the increase in the band gap and blue shift in the BPE-made  $\text{Cu}_2\text{O}$  was related to the decrease in particle size. Mott–Schottky analysis verified a moderate change in both carrier concentration and flat band potential among samples synthesized in the BPE process. The observed higher carrier concentration and flat band potential are related to the smaller particle size for samples that were synthesized at higher BPE voltage. These two factors allowed for improved total current generation.

As compared to the reference material,  $\text{Cu}_2\text{O}$  that was synthesized through BPE demonstrated an increase in photocurrent, a decrease in particle size, and a decrease in recombination at low potentials. However, a decrease in carrier concentration and flat band potential was observed, which was likely induced by the decrease in particle size and, therefore, crystallinity. Ultimately, this research demonstrates that the ideal conditions for BPE synthesis of  $\text{Cu}_2\text{O}$  have to be maintained at a high potential and for an extended duration of time in order to increase crystallite size. This could potentially minimize carrier recombination and increase photocurrent generation in BPE-generated oxides. Therefore, the conditions of bipolar synthesis can have a significant impact on  $\text{Cu}_2\text{O}$  crystal properties, as well as the ability to simultaneously maintain a green synthetic route, exclude hazardous waste products, and potentially create a scalable product. Further research is required in order to increase the photocurrent (e.g., pH, doping, complexing agents); all of which are known to have impacts on  $\text{Cu}_2\text{O}$  photocatalysis.

**Supplementary Materials:** The following are available online at <http://www.mdpi.com/2079-4991/9/12/1781/s1>. Figure S1: Schematic representing the bipolar electrochemical generation of copper ions for  $\text{Cu}_2\text{O}$  generation; Figure S2: (a) Color change of the reaction solution during BPE synthesis over 60 min, from left: 0 min, 10, 20, 30, 40, and 60 min (right photo). (b–g) Photos taken during progression of the reaction inside the bipolar cell; Figure S3: Refinement profile for the Rietveld analysis of room temperature XRD data that was collected for 4.5 V-3H and fitted to the model; Figure S4: Refinement profile for the Rietveld analysis of room temperature XRD data that was collected for 4.5 V-1H and fitted to the model; Figure S5: Refinement profile for the Rietveld analysis of room temperature XRD data that was collected for 5.0 V and fitted to the model; Figure S6: Refinement profile for the Rietveld analysis of room temperature XRD data that was collected for 6.0 V and fitted to the model; Figure S7: Refinement profile for the Rietveld analysis of room temperature XRD data that was collected for 7.0 V and fitted to the model; Figure S8: Refinement profile for the Rietveld analysis of room temperature XRD data that was collected for 8.0 V and fitted to the model; Figure S9: Emission spectra for  $\text{Cu}_2\text{O}$  synthesized by bipolar electrochemistry at 4.5 V (1 h); Figure S10: Emission spectra for  $\text{Cu}_2\text{O}$  synthesized by bipolar electrochemistry at 4.5 V (3 h); Figure S11: Emission spectra for  $\text{Cu}_2\text{O}$  synthesized by bipolar electrochemistry at 6.0 V (1 h); Figure S12: Emission spectra for  $\text{Cu}_2\text{O}$  synthesized by bipolar electrochemistry at 8.0 V (1 h); Figure S13: Emission spectra for commercial  $\text{Cu}_2\text{O}$ ; Figure S14: TEM of  $\text{Cu}_2\text{O}$  synthesized by bipolar electrochemistry for 1 h at 4.5 (a), 6.0 (b), 7.0 (c), and 8.0 V (d); Figure S15: TEM and SEM (inserts) of commercial  $\text{Cu}_2\text{O}$ .

**Author Contributions:** S.M., most of the experimental work and original draft preparation; C.D.F., editing and discussion; J.M., review and editing; A.U. and M.R., HRTEM analysis; R.A.W., photoluminescence and editing; D.C.A., Rietveld analysis, writing, and editing; A.I., writing, editing, supervision, project administration, and funding acquisition.

**Funding:** This project was funded by the NSERC Discovery Grant RGPIN-2016-03620 and the New Brunswick Innovation Foundation (NBIF). Financial support by the German Research Foundation (Inst 275/391-1) is gratefully acknowledged.

**Acknowledgments:** The authors would like to thank Steven Cogswell from the UNB Department of Biology, Microscopy and Microanalysis Laboratory for TEM and SEM imaging; Brian Titus, Michael Albright, and Adam Fowler (UNB) for their help in designing the bipolar electrochemical cell; Ven Reddy (UNB) for XRD analysis; Andrew George (Dalhousie) for XPS analysis; and Jared Mudrik (UofT) for diffusive reflectance analysis.

**Conflicts of Interest:** The authors declare no conflict of interest.

## References

1. Hussain, S.; Cao, C.; Usman, Z.; Nabi, G.; Butt, F.K.; Mahmood, K.; Ali, A.; Arshad, M.I.; Amin, N. Effect of films morphology on the performance of Cu<sub>2</sub>O PEC solar cells. *Optik* **2018**, *172*, 72–78. [[CrossRef](#)]
2. Deo, M.; Ogale, S. Crystal Facet Control for the Stability of p-Cu<sub>2</sub>O Nanoneedles as Photocathode for Photoelectrochemical Activity. *Mater. Today Proc.* **2018**, *5*, 23482–23489. [[CrossRef](#)]
3. Shyamal, S.; Hajra, P.; Mandal, H.; Bera, A.; Sariket, D.; Satpati, A.K.; Malashchonak, M.V.; Mazanik, A.V.; Korolik, O.V.; Kulak, A.I.; et al. Eu modified Cu<sub>2</sub>O thin films: Significant enhancement in efficiency of photoelectrochemical processes through suppression of charge carrier recombination. *Chem. Eng. J.* **2018**, *335*, 676–684. [[CrossRef](#)]
4. Baek, M.; Zafar, M.; Kim, S.; Kim, D.-H.; Jeon, C.-W.; Lee, J.; Yong, K. Enhancing Durability and Photoelectrochemical Performance of the Earth Abundant Ni-Mo/TiO<sub>2</sub>/CdS/CIGS Photocathode under Various pH Conditions. *ChemSusChem* **2018**, *11*, 3679–3688. [[CrossRef](#)]
5. Yang, Y.; Han, J.; Ning, X.; Su, J.; Shi, J.; Cao, W.; Xu, W. Photoelectrochemical stability improvement of cuprous oxide (Cu<sub>2</sub>O) thin films in aqueous solution. *Int. J. Energy Res.* **2016**, *40*, 112–123. [[CrossRef](#)]
6. Wong, T.K.S.; Zhuk, S.; Masudy-Panah, S.; Dalapati, G.K. Current Status and Future Prospects of Copper Oxide Heterojunction Solar Cells. *Materials* **2016**, *9*, 271. [[CrossRef](#)]
7. Dhaouadi, M.; Jlassi, M.; Sta, I.; Miled, I. Ben; Mousdis, G.; Kompitsas, M.; Dimassi, W. Physical Properties of Copper Oxide Thin Films Prepared by Sol-Gel Spin-Coating Method. *Am. J. Phys. Appl.* **2018**, *6*, 43–50. [[CrossRef](#)]
8. Arshadi-Rastabi, S.; Moghaddam, J.; Eskandarian, M.R. Synthesis, characterization and stability of Cu<sub>2</sub>O nanoparticles produced via supersaturation method considering operational parameters effect. *J. Ind. Eng. Chem.* **2015**, *22*, 34–40. [[CrossRef](#)]
9. Finney, E.E.; Finke, R.G. Nanocluster nucleation and growth kinetic and mechanistic studies: A review emphasizing transition-metal nanoclusters. *J. Colloid Interface Sci.* **2008**, *317*, 351–374. [[CrossRef](#)]
10. Zhou, D.; Li, Y.C.; Xu, P.; McCool, N.S.; Li, L.; Wang, W.; Mallouk, T.E. Visible-light controlled catalytic Cu<sub>2</sub>O–Au micromotors. *Nanoscale* **2017**, *9*, 75–78. [[CrossRef](#)]
11. Abhilash, M.R.; Akshatha, G.; Srikantaswamy, S. Photocatalytic dye degradation and biological activities of the Fe<sub>2</sub>O<sub>3</sub>/Cu<sub>2</sub>O nanocomposite. *RSC Adv.* **2019**, *9*, 8557–8568. [[CrossRef](#)]
12. Rezaei, S.; Landarani-Isfahani, A.; Moghadam, M.; Tangestaninejad, S.; Mirkhani, V.; Mohammadpoor-Baltork, I. Mono- and multifold C–C coupling reactions catalyzed by a palladium complex encapsulated in MIL-Cr as a three dimensional nano reactor. *RSC Adv.* **2016**, *6*, 92463–92472. [[CrossRef](#)]
13. Kefßler, M.T.; Robke, S.; Sahler, S.; Prechtel, M.H.G. Ligand-free copper(I) oxide nanoparticle-catalysed amination of aryl halides in ionic liquids. *Catal. Sci. Technol.* **2014**, *4*, 102–108. [[CrossRef](#)]
14. Sarkar, S.; Pal, R.; Roy, M.; Chatterjee, N.; Sarkar, S.; Sen, A.K. Nanodomain cubic copper (I) oxide as reusable catalyst for the synthesis of amides by amidation of aryl halides with isocyanides Swarbhenu. *Tetrahedron Lett.* **2015**, *56*, 623–626. [[CrossRef](#)]
15. Bhosale, M.A.; Sasaki, T.; Bhanage, B.M. A facile and rapid route for the synthesis of Cu/Cu<sub>2</sub>O nanoparticles and their application in the Sonogashira coupling reaction of acyl chlorides with terminal alkynes. *Catal. Sci. Technol.* **2014**, *4*, 4274–4280. [[CrossRef](#)]
16. Sharma, K.; Kumar, M.; Bhalla, V. Aggregates of the pentacenequinone derivative as reactors for the preparation of Ag@Cu<sub>2</sub>O core-shell NPs: An active photocatalyst for Suzuki and Suzuki type coupling reactions. *Chem. Commun.* **2015**, *51*, 12529–12532. [[CrossRef](#)]
17. Hu, X.E. Nucleophilic ring opening of aziridines. *Tetrahedron* **2004**, *60*, 2701–2743. [[CrossRef](#)]
18. Yao, Z.; Wei, X. Amidation of Aryl Halides Catalyzed by the Efficient and Recyclable Cu<sub>2</sub>O Nanoparticles. *Chin. J. Chem.* **2010**, *28*, 2260–2268. [[CrossRef](#)]
19. Pasini, D. The Click Reaction as an Efficient Tool for the Construction of Macrocyclic Structures. *Molecules* **2013**, *18*, 9512–9530. [[CrossRef](#)]
20. Kim, A.; Muthuchamy, N.; Yoon, C.; Joo, S.H.; Park, K.H. MOF-Derived Cu@Cu<sub>2</sub>O Nanocatalyst for Oxygen Reduction Reaction and Cycloaddition Reaction. *Nanomaterials* **2018**, *8*, 138. [[CrossRef](#)]
21. Mateo, D.; Albero, J.; Garcia, H. Photoassisted methanation using Cu<sub>2</sub>O nanoparticles supported on graphene as a photocatalyst. *Energy Environ. Sci.* **2017**, *10*, 2392–2400. [[CrossRef](#)]

22. Li, J.-Y.; Yuan, L.; Li, S.-H.; Tang, Z.-R.; Xu, Y.-J. One-dimensional copper-based heterostructures toward photo-driven reduction of CO<sub>2</sub> to sustainable fuels and feedstocks. *J. Mater. Chem. A* **2019**, *7*, 8676–8689. [[CrossRef](#)]
23. Munir, S.; Varzeghani, A.R.; Kaya, S. Electrocatalytic reduction of CO<sub>2</sub> to produce higher alcohols. *Sustain. Energy Fuels* **2018**, *2*, 2532–2541. [[CrossRef](#)]
24. Qu, Y.; Li, X.; Chen, G.; Zhang, H.; Chen, Y. Synthesis of Cu<sub>2</sub>O nano-whiskers by a novel wet-chemical route. *Mater. Lett.* **2008**, *62*, 886–888. [[CrossRef](#)]
25. Pathan, S.; Mishra, H.; Kachwala, S.; Nadar, S.; Marolikar, D.M.; Jha, M. Green Synthesis and Characterization of Cuprous Oxide Nanoparticles using Tea Extract. *SSRN Electron. J.* **2019**. [[CrossRef](#)]
26. Yan, D.; Li, S.; Hu, M.; Liu, S.; Zhu, Y.; Cao, M. Electrochemical synthesis and the gas-sensing properties of the Cu<sub>2</sub>O nanofilms/porous silicon hybrid structure. *Sens. Actuators B Chem.* **2016**, *223*, 626–633. [[CrossRef](#)]
27. Liu, C.; Chang, Y.-H.; Chen, J.; Feng, S.-P. Electrochemical Synthesis of Cu<sub>2</sub>O Concave Octahedrons with High-Index Facets and Enhanced Photoelectrochemical Activity. *ACS Appl. Mater. Interfaces* **2017**, *9*, 39027–39033. [[CrossRef](#)]
28. Tadjarodi, A.; Roshani, R. A green synthesis of copper oxide nanoparticles by mechanochemical method. *Curr. Chem. Lett.* **2014**, *3*, 215–220. [[CrossRef](#)]
29. Khayati, G.R.; Nourafkan, E.; Karimi, G.; Moradgholi, J. Synthesis of cuprous oxide nanoparticles by mechanochemical oxidation of copper in high planetary energy ball mill. *Adv. Powder Technol.* **2013**, *24*, 301–305. [[CrossRef](#)]
30. Yadav, S.; Jain, A.; Malhotra, P. A review on the sustainable routes for the synthesis and applications of cuprous oxide nanoparticles and their nanocomposites. *Green Chem.* **2019**, *21*, 937–955. [[CrossRef](#)]
31. Zhang, Q.B.; Hua, Y.X. Electrochemical synthesis of copper nanoparticles using cuprous oxide as a precursor in choline chloride–urea deep eutectic solvent: Nucleation and growth mechanism. *Phys. Chem. Chem. Phys.* **2014**, *16*, 27088–27095. [[CrossRef](#)] [[PubMed](#)]
32. Ongaro, M.; Gambirasi, A.; Ugo, P. Closed Bipolar Electrochemistry for the Low-Potential Asymmetrical Functionalization of Micro- and Nanowires. *ChemElectroChem* **2016**, *3*, 450–456. [[CrossRef](#)]
33. Fosdick, S.E.; Knust, K.N.; Scida, K.; Crooks, R.M. Bipolar Electrochemistry. *Angew. Chem. Int. Ed.* **2013**, *52*, 10438–10456. [[CrossRef](#)] [[PubMed](#)]
34. Macdonald-Clarke, C.J.; Martin, B.R.; McCabe, L.D.; McCabe, G.P.; Lachcik, P.J.; Wastney, M.; Weaver, C.M. Bioavailability of potassium from potatoes and potassium gluconate: A randomized dose response trial. *Am. J. Clin. Nutr.* **2016**, *104*, 346–353. [[CrossRef](#)] [[PubMed](#)]
35. Mikami, K.; Kido, Y.; Akaishi, Y.; Quitan, A.; Kida, T. Synthesis of Cu<sub>2</sub>O/CuO Nanocrystals and Their Application to H<sub>2</sub>S Sensing. *Sensors* **2019**, *19*, 211. [[CrossRef](#)] [[PubMed](#)]
36. Toby, B.H. EXPGUI, a graphical user interface for GSAS. *J. Appl. Cryst.* **2001**, *34*, 210–213. [[CrossRef](#)]
37. Larson, A.C.; von Dreele, R.B. General structure analysis system. *Los Alamos Natl. Lab. Rep. LAUR* **1994**, *96*, 86.
38. Foo, M.L.; Huang, Q.; Lynn, J.W.; Lee, W.-L.; Klimczuk, T.; Hagemann, I.S.; Ong, N.P.; Cava, R.J. Synthesis, structure and physical properties of Ru ferrites: BaMRu<sub>5</sub>O<sub>11</sub> (M=Li and Cu) and BaM'<sub>2</sub>Ru<sub>4</sub>O<sub>11</sub> (M'=Mn, Fe and Co). *J. Solid State Chem.* **2006**, *179*, 563–572. [[CrossRef](#)]
39. Howard, C.J. The approximation of asymmetric neutron powder diffraction peaks by sums of Gaussians. *J. Appl. Cryst.* **1982**, *15*, 615–620. [[CrossRef](#)]
40. Thompson, P.; Cox, D.E.; Hastings, J.B. Rietveld refinement of Debye-Scherrer synchrotron X-ray data from Al<sub>2</sub>O<sub>3</sub>. *J. Appl. Cryst.* **1987**, *20*, 79–83. [[CrossRef](#)]
41. Li, J.; Mei, Z.; Liu, L.; Liang, H.; Azarov, A.; Kuznetsov, A.; Liu, Y.; Ji, A.; Meng, Q.; Du, X. Probing Defects in Nitrogen-Doped Cu<sub>2</sub>O. *Sci. Rep.* **2014**, *4*, 7240. [[CrossRef](#)] [[PubMed](#)]
42. Biesinger, M.C. Advanced analysis of copper X-ray photoelectron spectra. *Surf. Interface Anal.* **2017**, *49*, 1325–1334. [[CrossRef](#)]
43. Zhu, C.; Oshero, A.; Panzer, M.J. Surface chemistry of electrodeposited Cu<sub>2</sub>O films studied by XPS. *Electrochem. Acta* **2013**, *111*, 771–778. [[CrossRef](#)]
44. Aria, A.I.; Kidambi, P.R.; Weatherup, R.S.; Xiao, L.; Williams, J.A.; Hofmann, S. Time Evolution of the Wettability of Supported Graphene under Ambient Air Exposure. *J. Phys. Chem. C* **2016**, *120*, 2215–2224. [[CrossRef](#)]
45. Pan, J.; Liu, G. Chapter Ten—Facet Control of Photocatalysts for Water Splitting. *Semicond. Semimet.* **2017**, *97*, 349–391.

46. He, P.; Shen, X.; Gao, H. Size-controlled preparation of Cu<sub>2</sub>O octahedron nanocrystals and studies on their optical absorption. *J. Colloid Interface Sci.* **2005**, *284*, 510–515. [[CrossRef](#)]
47. Pouloupoulos, P.; Baskoutas, S.; Pappas, S.D.; Garoufalis, C.S.; Droulias, S.A.; Zamani, A.; Kapaklis, V. Intense Quantum Confinement Effects in Cu<sub>2</sub>O Thin Films. *J. Phys. Chem. C* **2011**, *115*, 14839–14843. [[CrossRef](#)]
48. Niveditha, C.V.; Fatima, M.J.J.; Sindhu, S. Comprehensive Interfacial Study of Potentio-Dynamically Synthesized Copper Oxide Thin Films for Photoelectrochemical Applications. *J. Electrochem. Soc.* **2016**, *163*, 426–433. [[CrossRef](#)]
49. Hubička, Z.; Zlámál, M.; Čada, M.; Kment, Š.; Krýsa, J. Photo-electrochemical stability of copper oxide photocathodes deposited by reactive high power impulse magnetron sputtering. *Catal. Today* **2019**, *328*, 29–34. [[CrossRef](#)]
50. Dunn, H.K.; Feckl, J.M.; Müller, A.; Fattakhova-Rohlfing, D.; Morehead, S.G.; Roos, J.; Peter, L.M.; Scheu, C.; Bein, T. Tin doping speeds up hole transfer during light-driven water oxidation at hematite photoanodes. *Phys. Chem. Chem. Phys.* **2014**, *16*, 24610–24620. [[CrossRef](#)]
51. Kecsenovity, E.; Endrődi, B.; Tóth, P.S.; Zou, Y.; Dryfe, R.A.W.; Rajeshwar, K.; Janáky, C. Enhanced Photoelectrochemical Performance of Cuprous Oxide/Graphene Nanohybrids. *J. Am. Chem. Soc.* **2017**, *139*, 6682–6692. [[CrossRef](#)] [[PubMed](#)]



© 2019 by the authors. Licensee MDPI, Basel, Switzerland. This article is an open access article distributed under the terms and conditions of the Creative Commons Attribution (CC BY) license (<http://creativecommons.org/licenses/by/4.0/>).